

# Reduction of transport due to magnetic shear in gyrokinetic simulations of the scrape-off layer

N. R. Mandell<sup>1,2</sup>, G. W. Hammett<sup>3</sup>, A. Hakim<sup>3</sup>, M. Francisquez<sup>3</sup>

<sup>1</sup> MIT Plasma Science and Fusion Center, Cambridge, MA, 02139, USA

<sup>2</sup> Department of Astrophysical Sciences, Princeton University, Princeton, NJ 08543, USA

<sup>3</sup> Princeton Plasma Physics Laboratory, Princeton, NJ 08543, USA

E-mail: [nrm@mit.edu](mailto:nrm@mit.edu)

**Abstract.** The effect of varying magnetic shear on scrape-off layer turbulence and profiles is studied via electromagnetic gyrokinetic simulations of a helical scrape-off layer model. We develop a model helical geometry with magnetic shear and a corresponding field-aligned coordinate system, which is used for simulations with the GKEYLL code. We find that perpendicular transport is reduced in cases with stronger shear, resulting in higher peak particle and heat fluxes to the endplates. Electromagnetic effects slightly increase transport in strong shear cases.

*Keywords:* scrape-off layer turbulence, gyrokinetic simulation, magnetic confinement, magnetic shear, Gkeyll

Submitted to: *Plasma Phys. Control. Fusion*

## 1. Introduction

Developing a quantitative understanding of the mechanisms that control turbulence and transport in the tokamak edge and scrape-off layer (SOL) is important for the success of fusion. This region provides the boundary condition for the hot core and is also responsible for handling the power exhaust from the core. Mitigation strategies for the large heat loads in the SOL must be careful to avoid degrading the high core temperatures required to sustain a burning plasma [1]. Insights from theory and first-principles numerical modeling are important for solving these challenging issues. Significant progress has been made in modeling the edge and SOL using fluid [2, 3, 4, 5, 6, 7] and gyrokinetic [8, 9, 10, 11, 12, 13, 14, 15] models.

The geometry of the SOL in a diverted plasma can be challenging for turbulence modeling because field-aligned coordinate systems [16] (which are standard for core turbulence simulations) become singular due to the presence of the X point. While several gyrokinetic codes are now capable of handling X-point geometry by departing from field-aligned coordinates [8, 11, 15], implementation of X-point geometry in our efforts is left to future work. Instead, we aim here to study the fundamental impact of magnetic shear on scrape-off layer turbulence, since strong magnetic shear in the vicinity of the X point is a key feature of realistic SOL geometries. The local shear can approach  $\hat{s} = (r/q)dq/dr = 40$  one gyroradius away from the X point [17]. This results in significant radial shearing of eddies as one moves along the field line. In field-aligned coordinates, this is manifested by an increase in the radial mode number,  $k_x \propto \hat{s}$ , which in the large-aspect-ratio circular limit is given by  $k_x = k_y \hat{s}(\theta - \theta_0)$ , where  $\theta_0$  is the ballooning angle (the poloidal angle where the local  $k_x = 0$ ). The effects of magnetic shear on blob dynamics have been studied by [18] and [19]. They showed that strong shear can reduce the blob velocity by allowing cross-field currents to close through the thin sheared part of the blob, shorting out the blob polarization. This is a similar physical mechanism to the one that gives the well-known stabilizing effect of magnetic shear in ballooning mode theory for closed-field-line geometries [20]. Further, [17] showed that strong magnetic shear localized near X-points produces resistive X-point (RX) modes in both the (confined) edge and the SOL. These modes become disconnected across the X-point region, producing a fast-growing instability. As a result, the modes become disconnected from their boundary conditions, resulting in similar dynamics for both the edge and SOL. RX modes were found to be the dominant instability in L-mode conditions in [21, 22]. A theoretical investigation of strong magnetic shear near X points is also given in [23]. Note that in our studies we will not have localized

strong magnetic shear regions because we do not have X points, so we do not expect to see RX modes.

The GKEYLL code<sup>‡</sup> has recently become the first code to demonstrate the capability to simulate electromagnetic gyrokinetic turbulence on open magnetic field lines. Electromagnetic results have been shown in a simple helical SOL geometry with no magnetic shear [13, 24, 25, 26, 27]. Previous electrostatic GKEYLL results also used a helical geometry without shear, including studies of an NSTX-like helical SOL [12] and the Texas Helimak [28]. In this work we extend the geometry in GKEYLL to include magnetic shear and all other geometrical factors arising from using a non-orthogonal field-aligned coordinate system. We then include magnetic shear in full- $f$  electromagnetic gyrokinetic simulations with GKEYLL for the first time, taking a helical SOL geometry with magnetic shear and parameters that roughly approximate the SOL of the National Spherical Torus Experiment (NSTX).

The remainder of this paper is organized as follows: In Section 2, we describe the electromagnetic gyrokinetic model used for the simulations. We describe the helical SOL configuration, including magnetic shear, in section 3, along with details about the field-aligned coordinate system that we choose for this configuration. Section 4 presents the results of a parameter scan of the magnetic shear, showing electrostatic and electromagnetic simulations. The main result is that magnetic shear reduces transport, resulting in steeper profiles in cases with more shear. Conclusions are given in Section 5.

## 2. Gyrokinetic model

We model turbulence by solving the full- $f$  electromagnetic gyrokinetic (EMGK) system in the long-wavelength (drift-kinetic) limit. The gyrokinetic equation describes the evolution of the guiding-center distribution function  $f_s = f_s(\mathbf{R}, v_{\parallel}, \mu; t)$  for species  $s$ , where  $\mathbf{R} = (x, y, z)$  is the guiding-center position,  $v_{\parallel}$  is the parallel velocity, and  $\mu = m_s v_{\perp}^2 / (2B)$  is the magnetic moment. In conservative form we have

$$\begin{aligned} \frac{\partial(\mathcal{J}f_s)}{\partial t} + \nabla \cdot (\mathcal{J}\dot{\mathbf{R}}f_s) + \frac{\partial}{\partial v_{\parallel}} \left( \mathcal{J}\dot{v}_{\parallel}^H f_s \right) \\ - \frac{\partial}{\partial v_{\parallel}} \left( \mathcal{J} \frac{q_s}{m_s} \frac{\partial A_{\parallel}}{\partial t} f_s \right) = \mathcal{J}C[f_s] + \mathcal{J}S_s, \end{aligned} \quad (1)$$

<sup>‡</sup> <https://gkeyll.readthedocs.io>

where the nonlinear phase-space characteristics are given by

$$\dot{\mathbf{R}} = \frac{\mathbf{B}^*}{B_{\parallel}^*} v_{\parallel} + \frac{\hat{\mathbf{b}}}{qB_{\parallel}^*} \times (\mu \nabla B + q \nabla \Phi), \quad (2)$$

$$\dot{v}_{\parallel} = -\frac{\mathbf{B}^*}{mB_{\parallel}^*} \cdot (\mu \nabla B + q \nabla \Phi) - \frac{q}{m} \frac{\partial A_{\parallel}}{\partial t}, \quad (3)$$

with  $\Phi$  the electrostatic potential,  $A_{\parallel}$  the parallel magnetic vector potential. Collisions  $C[f_s]$  and sources  $S_s$  are included on the right-hand side of (1). Here,  $B_{\parallel}^* = \hat{\mathbf{b}} \cdot \mathbf{B}^*$  is the parallel component of the effective magnetic field  $\mathbf{B}^* = \mathbf{B} + (m_s v_{\parallel}/q_s) \nabla \times \hat{\mathbf{b}} + \delta \mathbf{B}$ , where  $\mathbf{B} = B \hat{\mathbf{b}}$  is the equilibrium magnetic field and  $\delta \mathbf{B} = \nabla \times (A_{\parallel} \hat{\mathbf{b}})$  is the perturbed magnetic field, neglecting compressional magnetic fluctuations. The Jacobian of the gyrocenter coordinates is  $\mathcal{J} = B_{\parallel}^*/m_s$ , and we make the approximation  $\hat{\mathbf{b}} \cdot \nabla \times \hat{\mathbf{b}} \approx 0$  so that  $B_{\parallel}^* \approx B$ . The species charge and mass are  $q_s$  and  $m_s$ , respectively. Note that we use the ‘‘symplectic’’ formulation [29] of electromagnetic gyrokinetics here, so that  $v_{\parallel}$  is used as a coordinate and the inductive component of the parallel electric field,  $\partial A_{\parallel}/\partial t$ , appears explicitly in (1).

The electrostatic potential is determined by the quasi-neutrality condition in the long-wavelength limit, which takes the form of the Poisson equation:

$$-\nabla \cdot (\epsilon_{\perp} \nabla_{\perp} \Phi) = \sum_s q_s \int f_s d^3 \mathbf{v}, \quad (4)$$

with  $d^3 \mathbf{v} = 2\pi dv_{\parallel} d\mu \mathcal{J}$  and

$$\epsilon_{\perp} = \sum_s \frac{m_s n_{0s}}{B^2}. \quad (5)$$

Here, we use a linearized polarization density  $n_0$  that we take to be a constant in time, which is consistent with neglecting a second-order  $E \times B$  energy term in the Hamiltonian. While the validity of this Boussinesq-type approximation in the SOL can be questioned due to large density fluctuations (and we plan to eventually improve on this approximation), a linearized polarization density is commonly used for computational efficiency [30, 12]. The magnetic vector potential is determined by the parallel Ampère equation,

$$-\nabla_{\perp}^2 A_{\parallel} = \mu_0 \sum_s q_s \int v_{\parallel} f_s d^3 \mathbf{v}. \quad (6)$$

Note that one can take the time derivative of (6) to obtain an exact Ohm’s law that can be used to solve for  $\partial A_{\parallel}/\partial t$  directly. For more details on the electromagnetic gyrokinetic system and our

implementation of the system in the GKEYLL code, see [13, 25].

To model the effect of collisions we use a conservative Lenard–Bernstein (or Dougherty) collision operator [31, 32],

$$\begin{aligned} \mathcal{JC}[f_s] = & \sum_r \nu_{sr} \left\{ \frac{\partial}{\partial v_{\parallel}} \left[ (v_{\parallel} - u_{\parallel sr}) \mathcal{J} f_s + v_{tsr}^2 \frac{\partial(\mathcal{J} f_s)}{\partial v_{\parallel}} \right] \right. \\ & \left. + \frac{\partial}{\partial \mu} \left[ 2\mu \mathcal{J} f_s + 2\mu \frac{m_s}{B} v_{tsr}^2 \frac{\partial(\mathcal{J} f_s)}{\partial \mu} \right] \right\}, \end{aligned} \quad (7)$$

where like-species collisions use  $u_{\parallel sr} = u_{\parallel s}$ ,  $v_{tsr} = v_{ts}$  and these quantities are given by

$$n_s u_{\parallel s} = \int v_{\parallel} f_s d^3 \mathbf{v}, \quad (8)$$

$$n_s u_{\parallel s}^2 + 3n_s v_{ts}^2 = \int (v_{\parallel}^2 + 2\mu B/m_s) f_s d^3 \mathbf{v}, \quad (9)$$

with  $n_s = \int f_s d^3 \mathbf{v}$  (see [33] for more details). Cross-species collisions among electrons and ions are also modeled [34]. This collision operator contains the effects of drag and pitch-angle scattering, and it conserves number, momentum and energy density. Consistent with our present long-wavelength treatment of the gyrokinetic system, finite-Larmor-radius effects are ignored. Note that in this model collision operator, the collision frequency  $\nu$  is velocity-independent, i.e.  $\nu \neq \nu(v)$ .

### 3. Helical SOL configuration with magnetic shear

The helical field in a simple magnetized torus (SMT) is given in cylindrical  $(R, \varphi, Z)$  coordinates (where  $\varphi$  is counter-clockwise viewed from above) by

$$\mathbf{B} = B_{\varphi} \hat{\boldsymbol{\varphi}} + B_v \hat{\mathbf{z}} = \frac{B_0 R_0}{R} \hat{\boldsymbol{\varphi}} + B_v \hat{\mathbf{z}}. \quad (10)$$

Note we can also write this as

$$\mathbf{B} = \nabla \Psi \times \nabla \varphi + B_0 R_0 \nabla \varphi, \quad (11)$$

with  $\Psi = R^2 B_v/2$  the vertical magnetic flux function (analogous to the poloidal flux in a tokamak). The field line pitch varies with radius, and can be expressed via

$$q(R) = \frac{H B_{\varphi}}{\pi R B_v} = \frac{B_0 R_0 H}{\pi R^2 B_v}, \quad (12)$$

where  $q$  is analogous to the safety factor in a tokamak, and  $H$  is the vertical height between the bottom and top end-plates where the field lines terminate. Here we have identified the poloidal length of the bad curvature region of a tokamak,  $\pi r$  (with  $r$  the minor radius) with the height  $H$ , so that our expression

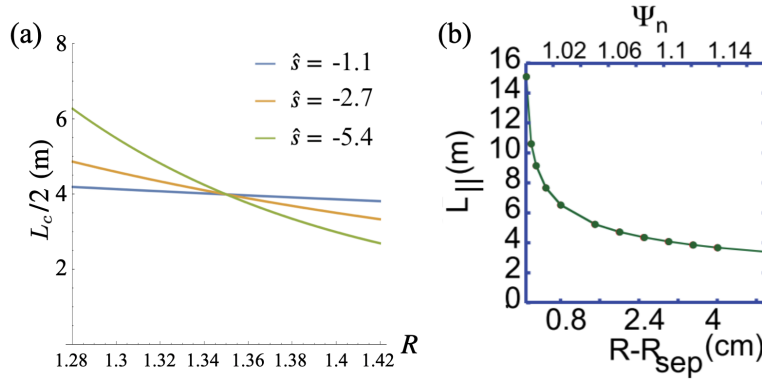


**Figure 1.** (a) Connection length,  $L_c/2 = HB/B_v/2$ , as a function of radius for several values of magnetic shear,  $\hat{s}$ , using NSTX-like parameters:  $R_0 = 0.85$  m,  $x_0 = R_0 + a = 1.35$  m,  $B_0 = 0.5$  T,  $H = 2.4$  m. Here we choose  $B_{v0}$  so that  $L_c(x_0) = 8$  m, which results in  $B_{v0} \approx 0.1$  T. (b) Connection length from the NSTX experiment,  $L_{\parallel}$ , defined as parallel length from midplane to lower divertor plate. Figure (b) reprinted from Boedo *et. al.*, *Phys. Plasmas* **21** 42309 (2014) [35], with the permission of AIP Publishing.

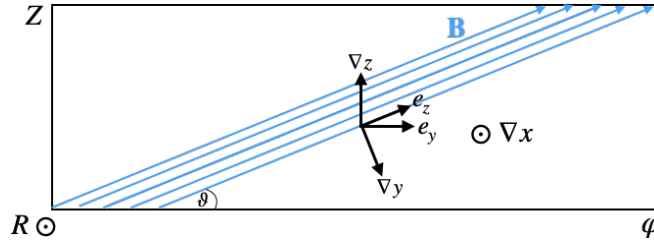


**Figure 2.** Diagram of field-aligned coordinate basis vectors in the  $(\varphi, Z)$  plane for a helical magnetic geometry. Note that vector magnitudes are not drawn to scale.

for  $q$  corresponds to the standard cylindrical tokamak expression  $q = (r/R)(B_\phi/B_\theta)$  with  $B_\phi$  and  $B_\theta$  the toroidal and poloidal components of the magnetic field in a tokamak. Similarly, we can define the magnetic shear as

$$\hat{s} = \frac{H}{\pi q} \frac{B_\varphi}{B} \frac{dq}{dR}, \quad (13)$$

which is analogous with the standard definition in a tokamak,  $\hat{s} = (r/q)dq/dr$ . Here, note that our definition of  $q$  is different by a factor of 2 from the expressions of [36], who effectively identify  $H$  with  $2\pi r$  in a tokamak. We also used different definitions of  $q$  and  $\hat{s}$  in [13]; we changed the definitions here for better correspondence with standard tokamak geometry.

If we allow the vertical field to have some simple radial dependence via  $B_v = B_v(R) = B_{v0}(R/x_0)^n$ , with  $x_0$  some major radius of interest, the shear is

$$\hat{s} = -\frac{H}{\pi R} \frac{B_\varphi}{B} (n+2). \quad (14)$$

When  $B_v = \text{const}$  ( $n = 0$ , as is the case for standard SMTs like the Helimak), we have  $\hat{s} = -2HB_\varphi/(\pi BR)$ . The connection length is given by  $L_c = HB/B_v$ , which in general varies with radius. In figure 1(a) we plot the connection length  $L_c$  as a function of radius for several values of  $\hat{s} = \{-1.1, -2.7, -5.4\}$  (corresponding to

$n = \{0, 3, 8\}$ ) with NSTX-like geometrical parameters (and evaluating  $\hat{s}$  at  $R = x_0$ ).

Note that here all quantities, including the field line pitch and the magnetic shear, are still constant *along* the field lines. This is in contrast to a real tokamak SOL, where the pitch and shear can vary significantly along the field lines, especially near the X-point due to flux expansion. The field line pitch at the midplane is also nearly constant with radius in a real tokamak SOL, while here we have the pitch varying with radius. Nonetheless, this simple geometry will still allow us to study some of the effects of magnetic shear. Comparing to the actual connection length in the NSTX experiment shown in figure 1(b) (with the figure adapted from Fig. 2 in [35]), we see that the variation in  $L_c$  with radius as  $|\hat{s}|$  increases is approaching the variation of the connection length in the experiment. However, in the experiment the connection length varies even more than in the  $\hat{s} = -5.4$  case over a shorter radial length, changing by a factor of almost four over a few centimeters.

### 3.1. Field-aligned coordinate system in helical geometry

In order to take advantage of the fact that turbulent structures are much more elongated along the field line

than perpendicular to it ( $k_{\parallel} \ll k_{\perp}$ ), we adopt a field-aligned coordinate system, which we will denote by  $(x, y, z)$ . To do this, we write the background magnetic field in Clebsch-like form as

$$\mathbf{B} = \mathcal{C}(x) \nabla x \times \nabla y, \quad (15)$$

where  $x$  and  $y$  are coordinates perpendicular to the background field, with  $x$  a radial-like coordinate, and  $y$  a field-line-labeling coordinate. This can be achieved by choosing the coordinates to be

$$x = R, \quad (16)$$

$$z = Z, \quad (17)$$

$$y = x_0 \left( \varphi - \frac{\pi q Z}{H} \right) = x_0 \left( \varphi - \frac{B_{\varphi} Z}{B_v R} \right). \quad (18)$$

The resulting gradient basis vectors are

$$\nabla x = \hat{\mathbf{R}}, \quad (19)$$

$$\nabla y = -\frac{\pi x_0 z}{H} \frac{dq}{dx} \hat{\mathbf{R}} + \frac{x_0}{x} \hat{\boldsymbol{\varphi}} - \frac{\pi x_0 q}{H} \hat{\mathbf{Z}}, \quad (20)$$

$$\nabla z = \hat{\mathbf{Z}}, \quad (21)$$

so that

$$\nabla x \times \nabla y = \frac{x_0}{x} \left( \frac{\pi q x}{H} \hat{\boldsymbol{\varphi}} + \hat{\mathbf{Z}} \right) = \frac{x_0}{x} \left( \frac{B_{\varphi}}{B_v} \hat{\boldsymbol{\varphi}} + \hat{\mathbf{Z}} \right). \quad (22)$$

Now taking  $\mathcal{C}(x) = B_v x / x_0$ , we obtain the correct form of the field,

$$\mathbf{B} = \frac{B_v x}{x_0} \nabla x \times \nabla y = B_{\varphi} \hat{\boldsymbol{\varphi}} + B_v \hat{\mathbf{Z}}. \quad (23)$$

A diagram of the field-aligned basis vectors in the  $(\varphi, Z)$  plane is shown in figure 2.

The Jacobian of the field-aligned coordinate system is

$$J = [(\nabla x \times \nabla y) \cdot \nabla z]^{-1} = \frac{x}{x_0}. \quad (24)$$

Note that we can write

$$\nabla y = \frac{B}{JB_v} \left( \hat{s} \theta \hat{\mathbf{R}} + \frac{B_v}{B} \hat{\boldsymbol{\varphi}} - \frac{B_{\varphi}}{B} \hat{\mathbf{Z}} \right), \quad (25)$$

where we have identified  $\theta = z\pi/H$ , so that

$$g^{yy} = |\nabla y|^2 = \left( \frac{B}{JB_v} \right)^2 (1 + \hat{s}^2 \theta^2). \quad (26)$$

§ Alternatively, we could have chosen the  $z$  coordinate to measure distance along the field line, with  $z = Z/\sin \vartheta = ZB/B_v$ . In this approach, the  $z$  domain extent is given by the connection length; however, the connection length can vary with radius, so the  $z$  domain extent would also need to vary with radius. Choosing the vertical height  $Z$  for the  $z$  coordinate does not have this issue (assuming the vertical height between the top and bottom end plates does not change with radius), so this is the approach that we take in this work.

This corresponds to the standard definition of  $g^{yy} = 1 + \hat{s}^2 \theta^2$  in a circular large-aspect-ratio tokamak, which confirms that we have made the appropriate definition of  $\hat{s}$ .

For more details about our implementation of the gyrokinetic system in a field-aligned coordinate system, see [25].

## 4. Results

In this section we present gyrokinetic simulations in the helical configuration with magnetic shear described above. The simulations were performed with the EMGK module of the GKEYLL plasma simulation framework. This module employs a discontinuous Galerkin (DG) discretization scheme for the EMGK system that conserves energy (in the continuous-time limit) and avoids the Ampère cancellation problem [13].

We perform a scan of the magnetic shear parameter, taking  $\hat{s} = \{-1.1, -2.7, -5.4\}$ , with the geometry becoming more sheared as  $|\hat{s}|$  increases. In each case, we perform both an electrostatic simulation and a simulation including electromagnetic effects. We use NSTX-like geometry parameters:  $R_0 = 0.85$  m,  $x_0 = R_0 + a = 1.35$  m,  $B_0 = 0.5$  T,  $H = 2.4$  m, and we choose  $B_{v0} = B_v(x_0)$  so that  $L_c(x_0) = 8$  m, resulting in  $B_{v0} \approx 0.1$  T. The resulting connection length as a function of radius is shown in figure 1. The simulation domain extents are taken to be  $1.26 \leq x \leq 1.42$  m ( $L_x \approx 56\rho_{s0}$ ) for the  $\hat{s} = -1.1$  and  $\hat{s} = -2.7$  case, and  $1.26 \leq x \leq 1.38$  ( $L_x \approx 42\rho_{s0}$ ) for the  $\hat{s} = -5.4$ , where we can use a smaller radial domain due to lower transport levels. The domain extents in the binormal and parallel directions, respectively, are  $-0.485 \leq y \leq 0.485$  m ( $L_y \approx 100\rho_{s0}H/L_c(x_0)$ ) and  $-H/2 \leq z \leq H/2$  in all cases. In velocity space, we use  $-4v_{ts} \leq v_{\parallel} \leq 4v_{ts}$  and  $0 \leq \mu \leq 6T_0/B_0$ , where  $v_{ts} = \sqrt{T_0/m_s}$  with  $T_0 = 40$  eV and  $B_0 = B_{\text{axis}}R_0/R_c$ .

The simulations use piecewise-linear ( $p = 1$ ) basis functions, with  $(N_x, N_y, N_z, N_{v_{\parallel}}, N_{\mu}) = (48, 96, 16, 10, 5)$  the number of cells in each dimension for the  $\hat{s} = -1.1, -2.7$  cases and  $(30, 96, 16, 10, 5)$  cells for the  $\hat{s} = -5.4$  case (which still gives slightly finer radial resolution than the other cases because the radial domain extent has also been reduced for  $\hat{s} = -5.4$ ). Note that for  $p = 1$  DG, one should double each of these numbers to obtain the equivalent number of grid-points for comparison with standard grid-based gyrokinetic codes. All other parameters are the same as used in the base case ( $\hat{n} = 1$ ) from [26], including the source power  $P_{\text{src}} = P_{\text{SOL}}L_y/(2\pi R_c) = 0.62$  MW and the source profile with a Gaussian peak at  $x = 1.3$  m. Boundary conditions are also the same as in [26], with Dirichlet boundary conditions  $\Phi = A_{\parallel} = 0$  on

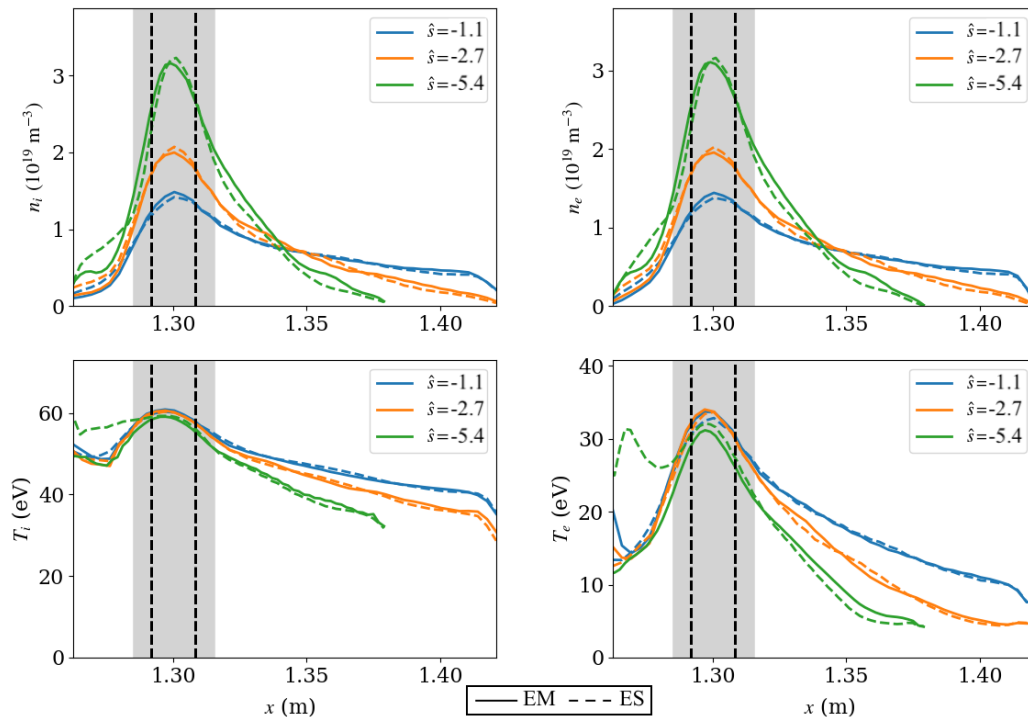


**Figure 3.** Time- and  $y$ -averaged midplane density and temperature profiles for several values of magnetic shear,  $\hat{s}$ , with ion quantities on the left and electron quantities on the right. Both electromagnetic (EM, solid lines) and electrostatic (ES, dashed) results are shown, with electromagnetic effects not having a significant effect on the profiles. The profiles steepen as  $|\hat{s}|$  increases and the geometry becomes more sheared.

the radial walls, periodic boundary conditions in the  $y$  direction, and conducting-sheath boundary conditions in the  $z$  direction. Our present sheath boundary condition does not account for the grazing incidence angle of the field lines on the endplates, which modifies the sheath physics [37] and the dynamics [38]. Instead we simply assume perpendicular incidence angle (as if the endplates were tilted appropriately at every incidence point) and leave more realistic Chodura sheath boundary conditions to future work.

In figure 3 we show time- and  $y$ -averaged density and temperature radial profiles for each case. Electromagnetic cases are shown with solid lines, while the electrostatic cases are shown dashed. The profiles for the  $\hat{s} = -1.1$  case are similar to the profiles from the base case in [26], which used a simplified geometry neglecting magnetic shear and assumed a constant connection length. This is somewhat expected since figure 1 shows that the connection length in the  $\hat{s} = -1.1$  case varies little over the domain. As we move to more sheared geometries, the density profiles steepen, with the peak midplane density more than doubling between the  $\hat{s} = -1.1$  and  $\hat{s} = -5.4$  cases. In all cases there is not much effect on the midplane profiles from including electromagnetic perturbations.

Snapshots of the electron density mapped to the  $(R, Z)$  plane for each of the electromagnetic cases are

shown in figure 4. We can clearly see that at large  $|Z|$  the turbulent structures are being tilted due to magnetic shear, with more tilting as  $|\hat{s}|$  increases. Near the midplane at  $Z = 0$ , the  $\hat{s} = -1.1$  case looks similar to the cases from [26], with blobs moving radially outwards and structures extending most of the width of the radial domain. On the other hand, the  $\hat{s} = -5.4$  case clearly shows evidence of reduced radial transport.

We can quantify this by computing the radial electron  $E \times B$  particle flux as

$$\Gamma_{\perp e} = \langle \tilde{n}_e \tilde{v}_r \rangle + \langle \tilde{u}_{\parallel e} \tilde{b}_r \rangle, \quad (27)$$

and the radial electron  $E \times B$  heat flux as

$$Q_{\perp e} = \langle \tilde{p}_e \tilde{v}_r \rangle + \langle \tilde{q}_{\parallel e} \tilde{b}_r \rangle. \quad (28)$$

Here, the first term is the contribution from the  $E \times B$  drift, with  $v_r = E_r/B = -(1/B)\partial\Phi/\partial y$ ,  $n_e$  the electron density,  $p_e$  the electron pressure. The second term is the flux due to magnetic flutter (for the electromagnetic cases only), with  $b_r = (1/B)\partial A_{\parallel}/\partial y$ ,  $u_{\parallel e}$  the electron parallel flow, and  $q_{\parallel e}$  the electron parallel heat flux. The tilde indicates the fluctuation of a time-varying quantity, defined as  $\tilde{F} = F - \bar{F}$  with  $\bar{F}$  the time average of  $F$ . The brackets  $\langle F \rangle$  denote an average in  $y$  and time. We plot these quantities, evaluated near the midplane, in figure 5 and

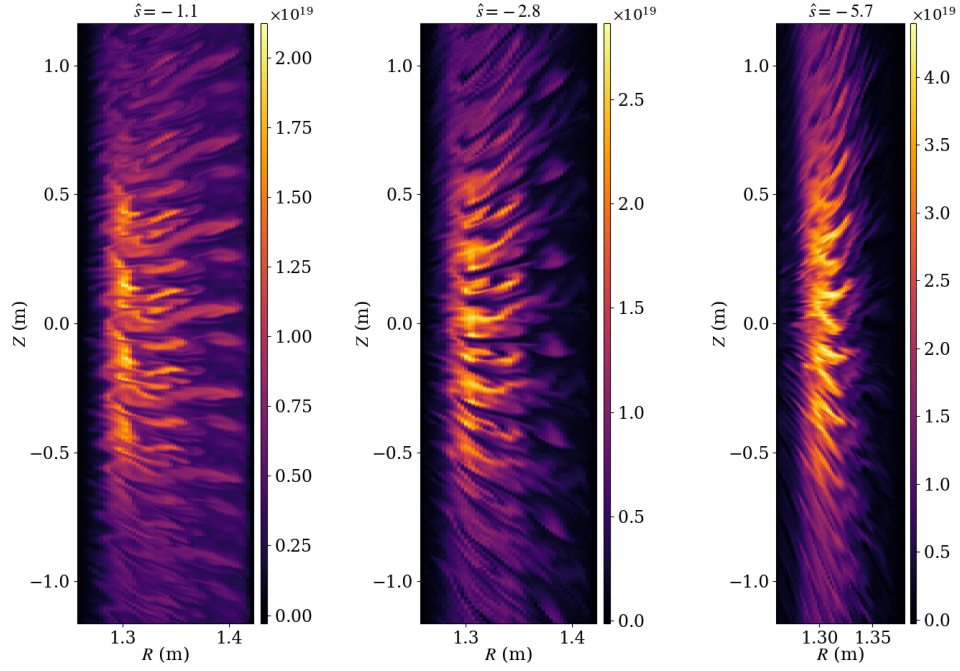


**Figure 4.** Snapshots of electron density (in  $\text{m}^{-3}$ ) mapped to the  $(R, Z)$  plane at  $t = 800 \mu\text{s}$  for the  $\hat{s} = -1.1, -2.7, -5.4$  electromagnetic cases.

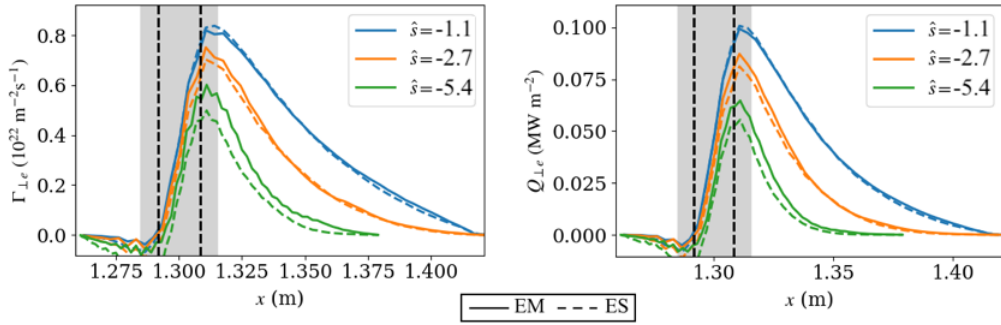


**Figure 5.** Radial electron  $E \times B$  particle flux (left) and heat flux (right) near the midplane, for both electromagnetic (solid) and electrostatic (dashed) cases. The cross-field transport decreases as the geometry becomes more sheared at larger  $|\hat{s}|$ , consistent with the steeper profiles seen in figure 3. Electromagnetic effects result in slightly increased transport in the stronger shear cases.

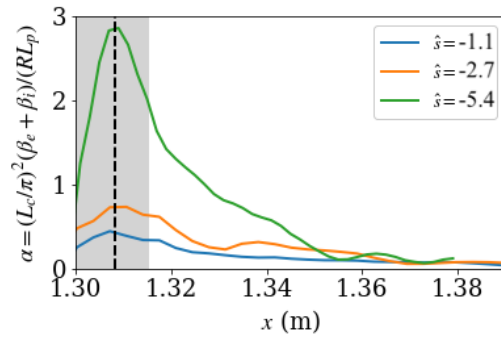


**Figure 6.** Radial profiles of the ballooning stability parameter  $\alpha = \gamma_{\text{int}}^2 / (k_{\parallel 0}^2 v_A^2) = (L_c/\pi)^2 (\beta_e + \beta_i) / (RL_p)$  at the midplane for each of the electromagnetic cases.

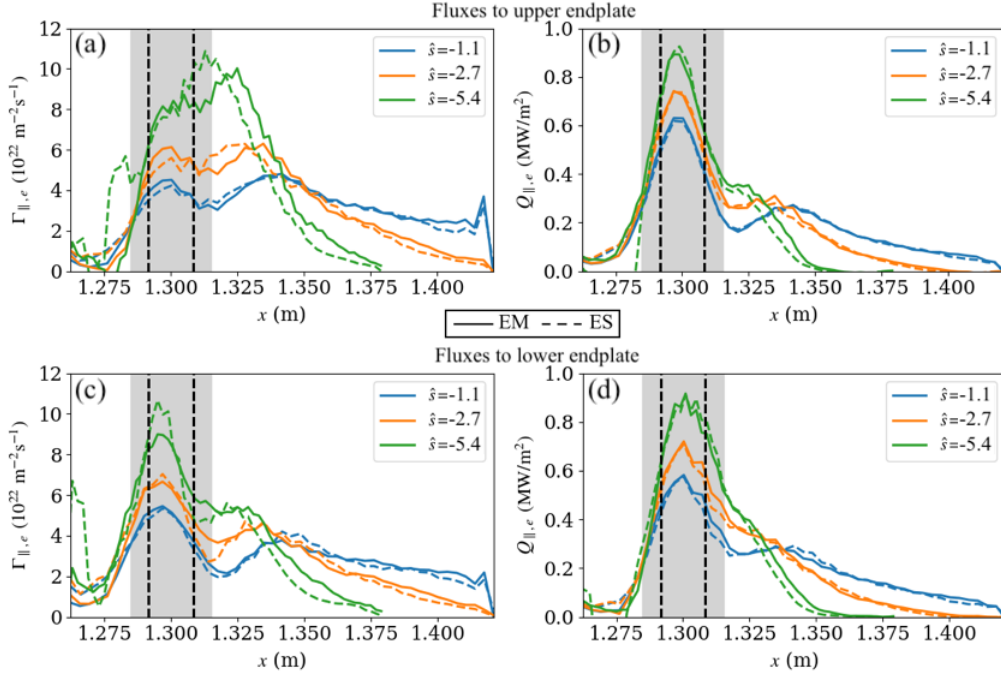


**Figure 7.** Time-averaged electron particle (left) and heat (right) fluxes to the upper (top row) and lower (bottom row) end plates. The peak fluxes increase as  $|\hat{s}|$  increases, consistent with less cross-field transport upstream.

confirm that indeed both particle and heat transport are reduced as  $|\hat{s}|$  increases.

Interestingly, despite the fact that we observed little change in the midplane profiles due to electromagnetic effects in figure 3, we see here that for the cases with more shear, electromagnetic effects are resulting in slightly more radial transport. Electromagnetic effects were also observed to increase transport in the no-shear simulations of [26], although in those cases, departure from the electrostatic limit required artificially increasing the source power to access a higher  $\beta$  regime. Here we have kept the nominal experimental  $P_{SOL}$  and yet we are still seeing the influence of electromagnetic effects on the radial transport. The key is that stronger magnetic shear results in steeper pressure profiles, which can strengthen interchange-ballooning instabilities via the ballooning stability parameter  $\alpha = \gamma_{int}^2 / (k_{||0}^2 v_A^2)$ , where  $k_{||0} = \pi / L_c$  is the longest parallel half-wavelength on the domain. Due to sheath and finite radial-mode-width effects, however, there is not a sharp limit on  $\alpha$  in the scrape-off layer [27]. Extension of the sheath-modified interchange-ballooning analysis in helical geometry presented in [27] to include magnetic shear is left to future work, but we do plot  $\alpha = \gamma_{int}^2 / (k_{||0}^2 v_A^2) = (L_c / \pi)^2 (\beta_e + \beta_i) / (R L_p)$  evaluated at the midplane in figure 6, where here  $k_{||0} = \pi / L_c$  itself varies with radius because of the variation of  $L_c$ . Taking the peak  $\alpha$  value from each the case, we have a range  $\alpha \approx 0.3 - 3$ , which is in the range of mea-

surements of  $\alpha$  in the near SOL of present experiments [39, 40, 41].

As a result of weaker cross-field transport, the peak particle and heat fluxes to the end plates increase in the cases with more shear, as shown in figure 7. Note that we have separately shown the fluxes to the upper (top row) and lower (bottom row) end plates. Despite the cross-field transport differences in the  $\hat{s} = -5.4$  case observed above, there is not much broadening of the flux profiles due to electromagnetic effects, although the peak particle flux to the lower endplate is slightly reduced. There are also some interesting asymmetries in the flux profiles between the ends. This is especially apparent in the particle flux in the stronger shear cases, where there is a noticeable shift in the profiles to higher  $x$  between the lower and upper plates. When we examine how the radial particle flux (taken just outside the source region near  $x = 1.32$  m) varies along the field line in figure 8, we see asymmetry as well. There is noticeably more radial transport at  $z > 0$  than  $z < 0$  for the  $\hat{s} = -5.4$  cases. This is consistent with the radial shift in the endplate particle fluxes to higher  $x$  between the lower and upper plates.

The average electron density also shows asymmetry along the field line, as shown in figure 9. Here we have again evaluated the profiles just outside the source region near  $x = 1.32$  m. There is a slight shift in the profiles to higher  $z$  in the  $\hat{s} = -5.4$  cases. One possible reason for the asymmetry is the presence of a



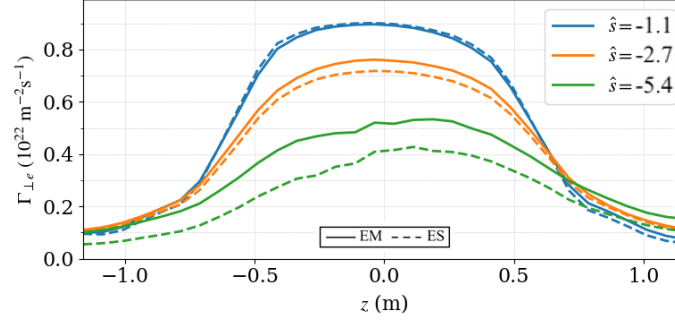


**Figure 8.** Time-averaged electron radial  $E \times B$  particle flux profiles along the field line, taken just outside the source region at  $x \sim 1.32$  m. In the  $\hat{s} = -5.4$  cases there is a noticeable asymmetry in the profiles, with slightly more radial transport at  $z > 0$  than  $z < 0$ . This is consistent with the differences in the particle fluxes to the bottom and top end plates shown in figure 7 (a) and (c).

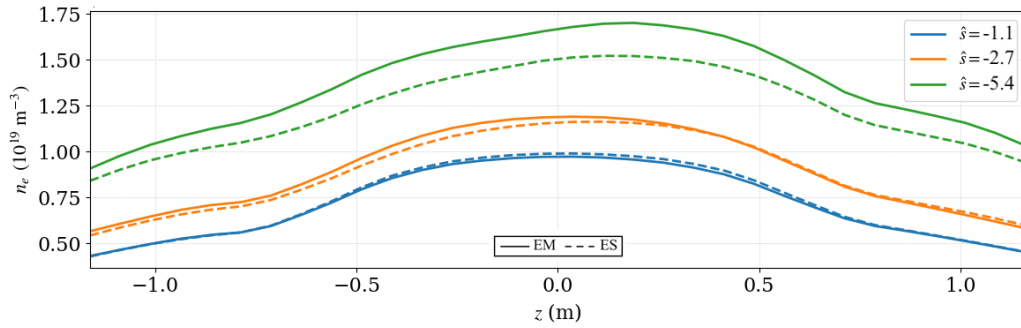


**Figure 9.** Time- and  $y$ -averaged electron density profiles along the field line, taken just outside the source region at  $x \sim 1.32$  m. There is noticeable asymmetric shift in the profiles in the  $\hat{s} = -5.4$  cases, with slightly higher density near the top of the domain ( $z = H/2 = 1.4$  m).

vertical component in the  $E \times B$  and magnetic drifts. For the  $E \times B$  drift, this is

$$\begin{aligned} \mathbf{v}_E \cdot \nabla z &= \frac{1}{JB} \left( b_x \frac{\partial \Phi}{\partial y} - b_y \frac{\partial \Phi}{\partial x} \right) \\ &= \frac{B_\varphi}{B^2} \left( -\frac{\partial \Phi}{\partial x} + \frac{x_0}{x} \frac{\pi}{H} \frac{B}{B_v} \hat{s} z \frac{\partial \Phi}{\partial y} \right) \end{aligned} \quad (29)$$

These vertical drift terms were not present in the simulations in [26], which used a simplified geometry in the  $B_v \ll B$  limit. It has been suggested that vertical drifts are responsible for asymmetry between top and bottom profiles in the Helimak [28].

## 5. Conclusions

In this paper we have explored the effects of magnetic shear on scrape-off layer transport. We first introduced shear into a helical SOL model geometry by taking the vertical field to be  $B_v \sim R^n$  so that the magnetic shear is proportional to  $-2 - n$ . We next derived a field-aligned coordinate system in this geometry that was implemented into the GKEYLL gyrokinetic code. We then performed electromagnetic and electrostatic gyrokinetic simulations in this geometry for several

values of  $\hat{s}$ . The results showed that magnetic shear reduces perpendicular transport, resulting in steeper radial profiles and higher peak fluxes to the endplates in cases with more shear. We also found that electromagnetic effects enhanced transport slightly (compared to corresponding electrostatic simulations) in the strong shear cases. Asymmetry in the endplate flux profiles between the top and bottom plates was found to be consistent with asymmetry in perpendicular transport about the device midplane; this is believed to be due to vertical components of the  $E \times B$  and magnetic drifts.

Extension of this work to modeling of a shaped scrape-off layer in a limiter configuration is already underway [25]. Of course, the eventual goal is to model diverted geometries with X points. This may require departure from field-aligned coordinate systems, at least in the immediate vicinity of the separatrix [8, 11, 15]. Nonetheless, this work was an important step towards modeling realistic SOL geometry with GKEYLL, which will enable closer comparison with experimental measurements.

## Acknowledgements

We would like to thank Tess Bernard, Petr Cagas, James Juno and other members of the GKEYLL team for helpful discussions and support, including the development of the `postgkyl` post-processing tool which facilitated the creation of many figures in this paper. Research support came from the U.S. Department of Energy: N.R.M. was supported by the DOE Fusion Energy Sciences Postdoctoral Research Program administered by the Oak Ridge Institute for Science and Education (ORISE) for the DOE via Oak Ridge Associated Universities (ORAU) under DOE contract number DE-SC0014664; G.W.H., A.H. and M.F. were supported by the Partnership for Multiscale Gyrokinetic Turbulence (MGK) and the High-Fidelity Boundary Plasma Simulation (HBPS) projects, part of the U.S. Department of Energy (DOE) Scientific Discovery Through Advanced Computing (SciDAC) program, via DOE contract DE-AC02-09CH11466 for the Princeton Plasma Physics Laboratory. Computations were performed on the Stellar cluster at Princeton University and the Cori cluster at NERSC. All opinions expressed in this paper are the authors' and do not necessarily reflect the policies and views of DOE, ORAU, or ORISE.

## Appendix A. Getting GKEYLL and reproducing results

Readers may reproduce our results and also use GKEYLL for their applications. The code and input files used here are available online. Full installation instructions for GKEYLL are provided on the GKEYLL website (<https://gkeyll.readthedocs.io>). The code can be installed on Unix-like operating systems (including Mac OS and Windows using the Windows Subsystem for Linux) either by installing the pre-built binaries using the conda package manager (<https://www.anaconda.com>) or building the code via sources. The input files used here are under version control and can be obtained from the repository at [https://github.com/ammarrhakim/gkyl-paper-inp/tree/master/2022\\_PPCF\\_EMGK\\_shear](https://github.com/ammarrhakim/gkyl-paper-inp/tree/master/2022_PPCF_EMGK_shear).

## References

- [1] Carter T, Baalrud S, Betti R, Ellis T, Foster J, Geddes C, Gleason A, Holland C, Humrickhouse P, Kessel C, Lasa A, Ma T, Mangi R, Schaffner D, Schmitz O, Shumlak U, Snead L, Solomon W, Trask E, Waelbroeck F, White A and Rej D 2020 Powering the Future: Fusion and Plasmas Tech. rep. FESAC
- [2] Xu X, Umansky M, Dudson B and Snyder P 2008 *Comm. Comput. Phys* **4** 949–979
- [3] Ricci P, Halpern F D, Jolliet S, Loizu J, Masetto A, Fasoli A, Furno I and Theiler C 2012 *Plasma Phys. Control. Fusion* **54** 124047
- [4] Halpern F D, Ricci P, Jolliet S, Loizu J, Morales J, Masetto A, Musil F, Riva F, Tran T M and Wersal C 2016 *J. Comput. Phys.* **315** 388–408 ISSN 10902716
- [5] Tamain P, Ghendrih P, Tsitrone E, Grandgirard V, Garbet X, Sarazin Y, Serre E, Ciraolo G and Chiavassa G 2010 *J. Comput. Phys.* **229** 361–378 ISSN 10902716
- [6] Zhu B, Francisquez M and Rogers B N 2018 *Comput. Phys. Commun.* **232** 46–58 ISSN 00104655
- [7] Stegmeir A, Coster D, Ross A, Maj O, Lackner K and Poli E 2018 *Plasma Phys. Control. Fusion* **60** 35005 ISSN 13616587 URL <https://doi.org/10.1088/1361-6587/aaa373>
- [8] Ku S H, Chang C S and Diamond P H 2009 *Nucl. Fusion* **49** 115021
- [9] Ku S H, Hager R, Chang C S, Kwon J M and Parker S E 2016 *J. Comput. Phys.* **315** 467–475 ISSN 10902716
- [10] Korpilo T, Gurchenko A D, Gusakov E Z, Heikkinen J A, Janhunen S J, Kiviniemi T P, Leerink S, Niskala P and Perevalov A A 2016 *Comp. Phys. Comm.* **203** 128–137 ISSN 00104655
- [11] Dorf M A, Dorr M R, Hittinger J A, Cohen R H and Rognlien T D 2016 *Phys. Plasmas* **23** 56102 ISSN 10897674
- [12] Shi E L, Hammett G W, Stoltzfus-Dueck T and Hakim A 2019 *Phys. Plasmas* **26** 012307 ISSN 10897674 (*Preprint* 1810.09500)
- [13] Mandell N R, Hakim A, Hammett G W and Francisquez M 2020 *J. Plasma Phys.* **86** ISSN 14697807 URL <https://doi.org/10.1017/S0022377820000070>
- [14] Pan Q, Told D, Shi E L, Hammett G W and Jenko F 2018 *Phys. Plasmas* **25** ISSN 10897674
- [15] Michels D, Stegmeir A, Ulbl P, Jarema D and Jenko F 2021 *Comput. Phys. Commun.* **264** 107986 ISSN 00104655 URL [www.elsevier.com/locate/cpc](http://www.elsevier.com/locate/cpc)
- [16] Beer M A, Cowley S C and Hammett G W 1995 *Phys. Plasmas* **2** 2687–2700 ISSN 1070664X
- [17] Myra J R, D'Ippolito D A, Xu X Q and Cohen R H 2000 *Phys. Plasmas* **7** 4622–4631 ISSN 1070664X URL <https://aip.scitation.org/doi/abs/10.1063/1.1314623>
- [18] D'Ippolito D A, Myra J R and Zweben S J 2011 *Phys. Plasmas* **18** 60501 ISSN 1070664X URL <https://doi.org/10.1063/1.3594609>

- [19] Krashenninnikov S I, D'Ippolito D A and Myra J R 2008 *J. Plasma Phys.* **74** 679–717 ISSN 00223778 URL <https://doi.org/10.1017/S0022377807006940>
- [20] Connor J W, Hastie R J and Taylor J B 1978 *Phys. Rev. Lett.* **40** 396
- [21] Xu X Q, Cohen R H, Rognlien T D and Myra J R 2000 *Phys. Plasmas* **7** 1951–1958 ISSN 10897674 URL <https://aip.scitation.org/doi/abs/10.1063/1.874044>
- [22] Xu X Q, Cohen H H, Porter G D, Rognlien T D, Ryutov D D, Myraa J R, D'Ippolito D A, Moyer R A and Groebner R J 2000 *Nucl. Fusion* **40** 731–736 ISSN 00295515 URL <https://iopscience.iop.org/article/10.1088/0029-5515/40/3Y/339>
- [23] Stoltzfus-Dueck T J 2009 *Tokamak edge turbulence and the approach to adiabatic response* Ph.D. thesis Princeton University
- [24] Hakim A H, Mandell N R, Bernard T N, Francisquez M, Hammett G W and Shi E L 2020 *Phys. Plasmas* **27** 042304 ISSN 10897674 URL <http://aip.scitation.org/doi/10.1063/1.5141157>
- [25] Mandell N R 2021 *Magnetic Fluctuations in Gyrokinetic Simulations of Tokamak Scrape-Off Layer Turbulence* Ph.D. thesis Princeton University (*Preprint* 2103.16062) URL <http://arxiv.org/abs/2103.16062>
- [26] Mandell N R, Hammett G W, Hakim A and Francisquez M 2021 (*submitted to Phys. Plasmas*) (*Preprint* 2112.06880) URL <https://arxiv.org/abs/2112.06880>
- [27] Mandell N R and Hammett G W (*in prep.*)
- [28] Bernard T N, Stoltzfus-Dueck T, Gentle K W, Hakim A, Hammett G W and Shi E L 2020 *Phys. Plasmas* **27** 62304 ISSN 10897674 URL <https://doi.org/10.1063/5.0003904>
- [29] Brizard A J and Hahm T S 2007 *Rev. Mod. Phys.* **79** 421–468 ISSN 00346861
- [30] Ku S H, Chang C S, Hager R, Churchill R M, Tynan G R, Cziegler I, Greenwald M, Hughes J, Parker S E, Adams M F, D'Azevedo E and Worley P 2018 *Phys. Plasmas* **25** 56107 ISSN 10897674
- [31] Lenard A and Bernstein I B 1958 *Phys. Rev.* **112** 1456–1459 ISSN 0031899X
- [32] Dougherty J P 1964 *Phys. Fluids* **7** 1788 ISSN 00319171
- [33] Francisquez M, Bernard T N, Mandell N R, Hammett G W and Hakim A 2020 *Nucl. Fusion* **60** 096021 URL <http://iopscience.iop.org/10.1088/1741-4326/aba0c9>
- [34] Francisquez M, Juno J, Hakim A, Hammett G W and Ernst D R 2021 (*submitted to Phys. Plasmas*) (*Preprint* 2109.10381) URL <http://arxiv.org/abs/2109.10381>
- [35] Boedo J A, Myra J R, Zweben S, Maingi R, Maqueda R J, Soukhanovskii V A, Ahn J W, Canik J, Crocker N, D'Ippolito D A, Bell R, Kugel H, Leblanc B, Roquemore L A and Rudakov D L 2014 *Phys. Plasmas* **21** 42309 ISSN 10897674 URL <https://doi.org/10.1063/1.4873390>
- [36] Perez J C, Horton W, Gentle K, Rowan W L, Lee K and Dahlburg R B 2006 *Phys. Plasmas* **13** 32101 ISSN 1070664X URL <https://doi.org/10.1063/1.2168401>
- [37] Chodura R 1982 *Phys. Fluids* **25** 1628–1633 ISSN 10706631 URL <https://doi.org/10.1063/1.863955>
- [38] Geraldini A, Parra F I and Militello F 2017 *Plasma Phys. Control. Fusion* **59** 025015 ISSN 13616587 URL <https://iopscience.iop.org/article/10.1088/1361-6587/59/2/025015>
- [39] Labombard B, Hughes J W, Smick N, Graf A, Marr K, McDermott R, Reinke M, Greenwald M, Lipschultz B, Terry J L, Whyte D G and Zweben S J 2008 *Phys. Plasmas* **15** 56106 ISSN 1070664X URL <https://doi.org/10.1063/1.2838246>
- [40] Eich T, Goldston R J, Kallenbach A, Sieglin B and Sun H J 2018 *Nucl. Fusion* **58** 034001 ISSN 17414326 URL <https://iopscience.iop.org/article/10.1088/1741-4326/aaa340>
- [41] Eich T and Manz P 2021 *Nucl. Fusion* **61** 086017 ISSN 17414326 URL <https://iopscience.iop.org/article/10.1088/1741-4326/ac0412>